A Variable Reluctance based Planar Dual Coil Angle Sensor with Enhanced Linearity

Anil Kumar Appukuttan Nair Syamala Amma, Narayanan Peringode Pisharam , Jeshma Thalapil Vaheeda, and Sreenath Vijayakumar, *Member, IEEE*

***Abstract*—An easy-to-fabricate, full circle range (0°-360°), planar coil-based variable reluctance (VR) angle transducer with enhanced linearity is presented in this paper. The proposed sensor system aims to mitigate the limitations of existing VR angle sensors, particularly their limited accuracy and nonlinearity, resulting from the inherent sensor output characteristics. By carefully designing the coil geometry to achieve uniform flux distribution and implementing a simple semicircular-shaped rotor, the sensor system offers enhanced performance and linearity. The proposed sensor employs a semi-circular-shaped rotor plate (RP) placed between two PCBs with four coils each. These coils are strategically designed to ensure a linear variation of inductance with respect to the RP position, resulting in improved linearity in the sensor output. After validating the sensor design through analytical methods and finite element analysis (FEA), a suitable algorithm was developed for accurately estimating the rotor angle. A sensor prototype was manufactured to evaluate the performance of the sensor system. The prototype showed an excellent linearity with a worst case error of 0.31% and a resolution of 0.11°. The sensor shows negligible sensitivity to axial misalignment of the shaft and the presence of external magnetic objects, highlighting the practical usefulness of the system.**

***Index Terms*—angle sensor, variable reluctance, planar coils, ratio-metric, inductance, dual coil.**

I. Introduction

Non-contact angle sensors are extensively used in automotive, robotic, biomedical and industrial applications [1]–[5]. Depending on the application, the requirements on sensitivity, resolution, robustness, cost, and ease of manufacturability may vary [2] . In automotive applications, achieving high accuracy, robustness, and reliability at an affordable cost with a simplified manufacturing process remains a primary concern [1], [2]. Very often, the angle sensors used in automotive applications must meet stringent regulations in terms of accuracy, temperature range, and tolerance to vibrations [1]. Furthermore, they must withstand harsh and hostile environmental conditions, and their output should be insensitive to dust, oil, humidity, and other interferences [1], [2]. Notable applications of angle sensors within the automotive domain include throttle positioning, steering wheel rotation sensing, accelerator pedal position sensing, etc. [2].

The literature shows a wide variety of non-contact angle sensors employing diverse operating principles: capacitive, optical, inductive, hall-effect, and magnetoresistive sensing techniques [2], [4], [6]–[10]. Despite their cost-effectiveness, low power consumption, and minimal maintenance requirements, capacitive sensors are unsuitable for use in harsh environments containing oil, dirt, and moisture [2]. Although optical sensors offer high accuracy and resolution, they cannot be deployed in dusty environmental conditions [2], [11]. In contrast, magnetic angle sensors (inductive, eddy current, VR, hall-effect, and magnetoresistive sensing techniques) are considered the right choice because of their reliable performance, even in harsh and hostile environments [1], [2], [12]. The outputs of the magnetic sensors are insensitive to moisture, grease, dust, oil, etc [1], [2], [12]. In recent years, variable reluctance-based angle sensors have gained attention for their simplicity, robustness, low cost, and suitability for operation in harsh environments [2]. Variable reluctance (VR)-coil based sensing [13]–[15] is an extensively used angular measurement technique that has gained new dimensions due to the development of planar coil technologies. Although rotary variable differential transformer (RVDT) [12], [16] and resolvers [16] are absolutely mature and famous inductive sensing technologies, recent research focuses on planar coil-based low-cost angle sensing schemes [12], [14], [17]. Planar coils offer cost-effective manufacturing solutions and are suitable for space-constraint applications [12], [14], [17].

One of the main shortcomings of existing variable reluctance-based angle sensors is their limited accuracy and nonlinearity, which stem from the inherent nonlinearity of the sensor's output [10], [14], [18], [19]. Additionally, the complex shape of the rotor in VR angle sensors poses several challenges that must be addressed in sensor design and operation [13], [16], [19] . Firstly, the non-uniform variations in magnetic reluctance induced by the complex-shaped rotor can lead to non-linearities in the sensor's output and complicate signal interpretation. This also leads to an increased complexity of signal processing algorithms required to accurately extract angular position information from the sensor signals. Furthermore, the non-uniform flux distribution of the coils used in VR angle sensors due to the geometry of these coil windings can lead to variations in sensor sensitivity and linearity [13], [14], [16], [19]. Optimising both the coil geometry and rotor shape in VR angle sensors can result in significant improvements in sensor performance.

Anil Kumar Appukuttan Nair Syamala Amma is with the School of Engineering, The University of Edinburgh, EH8 9YL, UK (e-mail: aappukut@ed.ac.uk)

Narayanan Peringode Pisharam and Sreenath Vijayakumar are with the Department of Electrical Engineering,Indian Institute of Technology Palakkad, Kerala 678623, India (e-mail: 122004005@smail.iitpkd.ac.in; sreenath@iitpkd.ac.in).

Jeshma Thalapil Vaheeda is with the School of Engineering, Computing and Mathematics, Oxford Brookes University, OX3 0BP, UK (e-mail: jthalapilvaheeda@brookes.ac.uk)

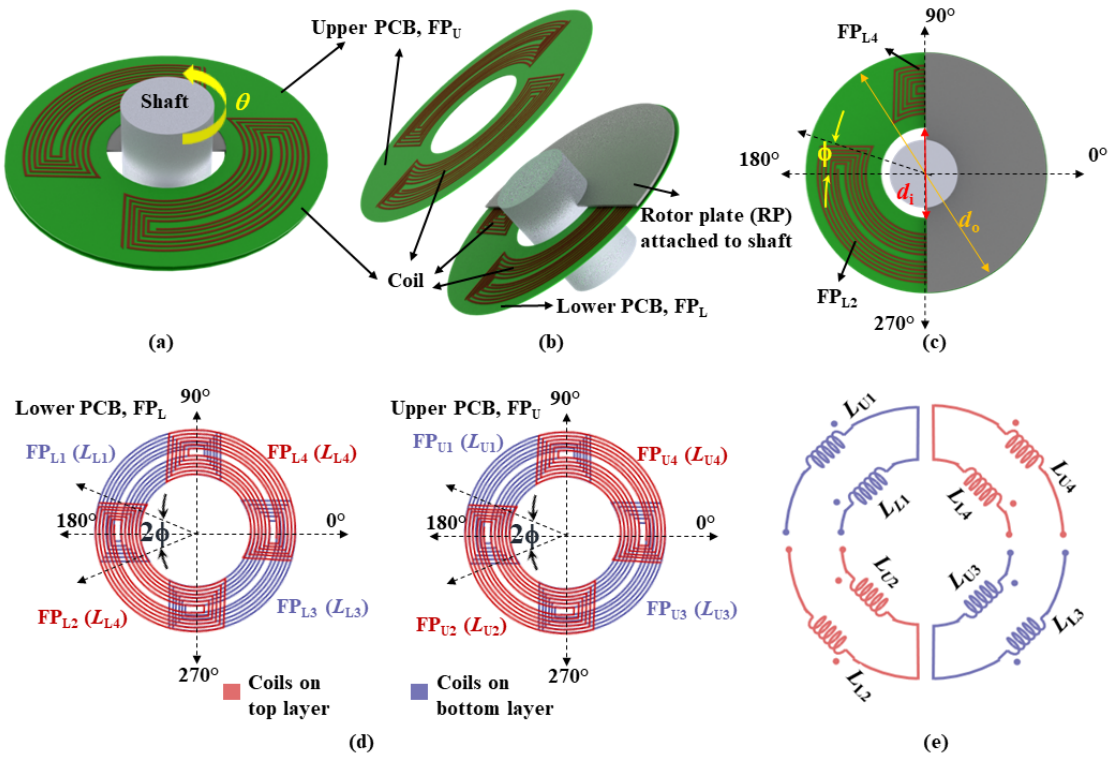

Fig. 1. A graphical representation of the proposed sensor. (a) A complete view of the assembled sensor prototype. (b) Exploded view to see the internal structure. The rotor plate (RP) in semi-circular shape is positioned in between the fixed PCBs, FP_U and FP_L that are laid parallel to each other. The coils on the bottom layer of FP_U and FP_L are obstructed in this view. (c) The top view of the relative positioning of FP_L and RP is shown. The 0° reference position of RP for angle measurement is marked. The inner diameter (d_i) and outer diameter (d_o) of the fixed plate is shown. (d) The coil arrangement in FP_L and FP_U is shown. The coils on the top layer of the fixed plates, FP_L and FP_U are shown in red color, and the ones on the bottom are shown in blue. The inductance of the coils in FP_L is represented by L_{L1}-L_{L4} and in FP_U, it is represented by L_{U1}-L_{U4}. (e) The connection diagram of the corresponding coils in FP_L and FP_U is shown.

This article presents a novel and simple way of measuring the planar angle by employing the combined features of the planar coil and variable reluctance-based sensing mechanism. In the proposed sensor, significant steps have been taken to address the challenges associated with non-uniform flux distribution in variable reluctance (VR) angle sensors. Specifically, we have designed a coil with carefully desiogned geometry to achieve uniform flux distribution across the sensing area. Additionally, we have implemented a simple shape for the rotor with a semicircular profile to further enhance sensor performance. This ensured that the inductances of these coils were modulated linearly with respect to the angular position of the shaft. The sensor system is thin and small with a measurement range of 0° to 360°. In the following section, a description of the proposed sensor system and its working principle is provided. Simulation studies conducted by finite element method to validate the sensor design is presented in Section III. A laboratory scale prototype was built to test the functionality of the system, which is described in detail in Section IV. The experimental results obtained are also presented in this section. Section VI concludes the discussion with the main findings found from the testing of the sensor system.

II. Proposed Sensor System

Fig. 1 illustrates the structural details of the proposed sensor, and Fig. 1(b) shows the exploded view of the proposed sensor. The system details and the working principle are described in the following sections.

A. System Details

The proposed angle sensor has a fixed part that comprises two parallel PCBs, Fixed Plate Upper (FP_U) and Fixed Plate Lower (FP_L) in the shape of annular discs. These PCBs are mounted parallel to each other as shown in Fig. 1(b). Each of the fixed plates has four partially overlapping planar coils each that are placed 90° apart as shown in Fig. 1(c) and (d). Each planar coil is in the shape of an annulus sector (sector of concentric circles) that covers an angle of $90^\circ + 2\phi$ (Fig. 1(c) and (d)) and is placed such that there is an area of overlap of 2ϕ between each pair of adjacent coils. The overhang, ϕ, should have a minimum value such that the coil ends do not affect the linear variation of coil inductance in the desired quadrants which is described in detail in Section III. To accommodate the overlap between the coils, the four coils within the PCB are arranged in two layers (two coils on top and two on bottom) of the PCB, such that the coils positioned opposite each other are on the same layer. This is shown in

Fig. 1(d), where the red coils are on the top layer, and the blue coils are on the bottom layer.

The four coils on FP_U are designated as FP_{U1} to FP_{U4}, and their counterparts on FP_L are designated as FP_{L1} to FP_{L4}. FP_U and FP_L are positioned in parallel to each other, ensuring that the corresponding coils on them are precisely aligned with each other. In addition, each coil in fixed plate upper (FP_{Ui}) and its corresponding coil in fixed plate lower (FP_{Li}) are connected together in an anti-series manner forming a single coil FP_i ($1 \leq i \leq 4$) having an effective inductance of L_i ($1 \leq i \leq 4$) as shown in Fig. 1(e). Overall, in the top view, the four coils in each of the parallel discs, FP_U and FP_L, will give an impression of being situated at the edge of a circle continuously with a slight overlap between adjacent coils.

For the PCB design, the inner diameter (d_i) can be decided according to the shaft diameter. The inner diameter (d_o) depends on the available radial installation space. From this, the width of the PCB, W, can be calculated using $W = (d_o - d_i)/2$. Once W is decided, the number of coil turns of the individual coils on PCB can be calculated. The sensitivity of the sensor output increases with the number of coil turns. However, with a fixed W, the number of turns is limited by the tolerance of the available PCB fabrication facility. Also, as the number of coil turns is increased, the track width has to be decreased accordingly, which in turn, will increase the coil resistance. Therefore it is recommended to keep an optimum balance between the performance and the system design complexities.

The rotating part of the sensor, denoted as RP, is fabricated using a high-permeability material and takes the shape of a semicircle. The RP is placed in between FP_U and FP_L, firmly fitted to the rotating shaft whose angle, θ, is to be measured. The reference position of RP for angle measurement is shown in Fig. 1(c). For the rotor plate, RP, the outer diameter is equal to the outer diameter of the PCB. The inner diameter is again restricted by the shaft diameter of the installation. In the prototype, RP was manufactured using mu-metal sheets of relative permeability 40,000. For low cost applications, one may use magnetic materials of lower relative permeability as the error introduced is negligible, as mentioned in Section III-D.

B. Methodology

The coils within each PCB are energized using sinusoidal signals, generating magnetic fields around them. When θ changes, this causes a change in the position of the RP with respect to each coil. This means that the area of overlap (A_m) between each coil and RP changes as a function of θ. This in turn, varies the reluctance offered by the magnetic circuit that varies the effective inductance of the coil. Therefore, the variation in A_m can be used to sense the change in angular position.

To understand the variation in reluctance as a function of θ, the mathematical expression of the variation in A_m of a single coil, FP_{L1} on FP_L with respect to the rotation of the RP, was derived from Fig. 2.

Fig. 2 shows one of the coils on FP_L denoted as FP_{L1}. For the given coil-rotor arrangement (coil is in the second quadrant), let the inductance of the coil FP_{L1} be represented as $L_{L1}(\theta)$. Let the inner radius of this coil be r_i, and the outer radius be r_o. The area of overlap at an angle θ, $A_m(\theta)$ is given by,

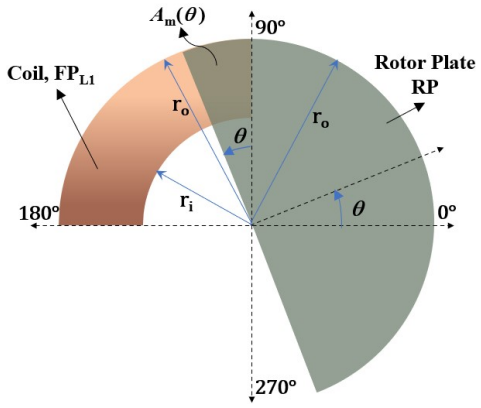

Fig. 2. Graphical representation of the top view of a coil in the FP_L and the movable rotor plate at an angle θ. The area of overlap at angle θ is shown.

$$A_m(\theta) = \begin{cases} \dfrac{\theta}{360^\circ} \times \pi(r_o^2 - r_i^2), & 0^\circ < \theta \leq 90^\circ \\ \dfrac{90^\circ}{360^\circ} \times \pi(r_o^2 - r_i^2), & 90^\circ < \theta \leq 180^\circ \\ \dfrac{(270^\circ - \theta)}{360^\circ} \times \pi(r_o^2 - r_i^2), & 180^\circ < \theta \leq 270^\circ \\ 0, & 270^\circ < \theta \leq 360^\circ \end{cases} \tag{1}$$

As the area of overlap ($A_m(\theta)$) between the coil and the RP is a function of the rotor angle, θ, the coil inductance L_{L1} also shows a similar variation with respect to θ. Using (1), as θ is varied between 0° to 360°, $L_{L1}(\theta)$ increases in $0^\circ < \theta \leq 90^\circ$ and decreases in $180^\circ < \theta \leq 270^\circ$ (due to the proportional variation in $A_m(\theta)$). However, $L_{L1}(\theta)$ remains constant in the range $90^\circ < \theta \leq 180^\circ$ and $270^\circ < \theta \leq 360^\circ$. Therefore, if we consider a coil capable of generating a uniform flux density throughout the region $0^\circ \leq \theta \leq 90^\circ$, the coil's inductance can be derived as a proportional function of the area of overlap between the coil and the core. When one or more parallel conductors carry the same current, it will generate a uniform magnetic flux density along the direction of current flow. This property is utilized to achieve a uniform magnetic flux density across the region. However, when winding a coil, the adjacent wires must be connected to form a complete coil, leading to a non-uniform magnetic field density at both ends of the coil. Therefore, to get a linear variation for $L_{L1}(\theta)$ against θ in the range $0^\circ < \theta \leq 90^\circ$ and $180^\circ < \theta \leq 270^\circ$, the coil was placed such that it extends from $(90^\circ - \phi)$ to $(180^\circ + \phi)$ with a slight overhang, ϕ on its either ends. This is to ensure that the variation in coil geometry at the coil ends doesn't alter the linear inductance variation in the region of interest ($0^\circ < \theta \leq 90^\circ$ and $180^\circ < \theta \leq 270^\circ$).

From a single coil, it was possible to get a linear variation of inductance against θ in the range of $0^\circ < \theta \leq 90^\circ$ and $180^\circ < \theta \leq 270^\circ$. By using four coils placed 90° apart, the

measurement range could be extended to a full circle range of 0°-360°.

To get the actual inductance variation of the coils against θ and to analyze the sensor characteristics from the inductance values, a finite element analysis (FEA) is conducted, which will be discussed in the following section.

III. Finite Element Analysis (FEA)

To obtain the inductance variation against θ of the sensor system, a finite element analysis (FEA) of the sensor was carried out using the ac/dc module (magnetic fields) of the COMSOL Multiphysics software.

Initially, the FEM analysis was performed on a single coil, FP_{L1} as given in Fig. 3 to understand the effects of coil ends. The coil was modeled as an annulus sector with an inner diameter of 60 mm and an outer diameter of 95 mm having 20 turns. It covered a sector angle of 90 °+2ϕ where ϕ was set as 20 °. The coil inductance was found to be 27 µH with a resistance of 0.1 Ω. The coil was energised using 1 kHz, 100 mA (rms) current source. The flux density distribution of this coil will be as shown in Fig. 3(a). It can be seen that the flux density generated by this coil has a uniform spatial distribution in the region 90°-180°. The flux density at the coil ends shows a variation in the pattern from that observed in 90°-180°. an overhang angle, ϕ of 20 ° was intentionally introduced, to avoid this effect of the coil ends in the inductance measured (in the range 0°-90° and 180°-270°). This ensured that the coil inductance varied linearly when RP was moved in the range 0°-90° and 180°-270°.

To study the change in inductance with respect to θ, a semicircular shaped rotor plate (RP) of diameter 100 mm having a μ_r of 4000 was used. RP was moved in steps of 10° and the inductance value of the coil was recorded in each step. The change in inductance obtained from the FEM analysis is shown in Fig. 3(b). As θ increases from 0 ° to 90 °, the area of overlap between RP and coil increases, which in turn, increases the amount of interaction of the magnetic field with RP. As a result, the coil inductance increases linearly against θ in 0°-90°. Similarly, the magnetic interaction between the coil and RP decreases in the range of 180°-270°, and therefore, the curve shows a decrease in inductance. It was also observed from the simulation studies, that the characteristics obtained in Fig. 3(b) was valid only if the RP was in the shape of a semicircle.

A. Number of Coils

A single coil exhibits a linear variation in its inductance against θ in 0°-90° and 180°-270° range; however, it does not provide sufficient information to determine the angle in other quadrants, i.e., 90°-180° and 270°-360° (see Fig. 3(b)). Additionally, ambiguity arises due to obtaining the same inductance value for two θ positions, one at ($0° < \theta \leq 90°$) and another at ($180° < \theta \leq 270°$). To get the information on θ for a full-circle range ($0° \leq \theta \leq 360°$), in the proposed sensor system, four identical planar coils, FP_{L1}, FP_{L2}, FP_{L3}, and FP_{L4}, in the shape of an annulus sector were designed. The four coils were spatially arranged 90° apart on a PCB

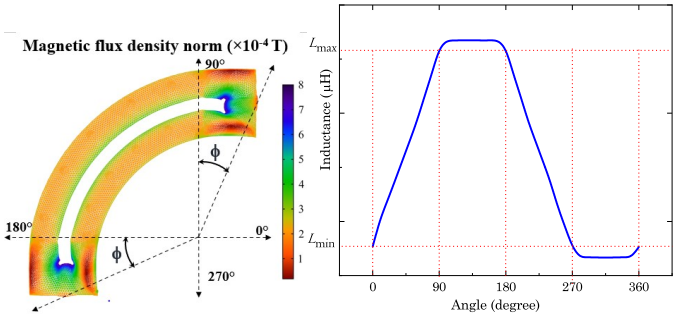

Fig. 3. (a) Flux density waveform for a single coil, FP_{L1} carrying a current of 100 mA. (b) The variation of a single coil inductance against θ.

along the edge of a circle with a slight overlap (2ϕ) between the coils as shown in Fig. 1 (d). This arrangement could extend the range of angle measurement from 0° to 360° which will be discussed in Section III-B.

B. Dual Coil/PCB Arrangement

A dual coil arrangement was employed for each of the coils due to the following reasons:

1) Sensitivity: As shown in Fig. 1, the four coils on the PCB, FP_L, are arranged on both the top and bottom sides of the PCB to avoid overlapping between adjacent coils. The rotating plate RP is placed above the top layer of FP_L with a minimal air gap. Consequently, the distance between the rotating plate and the coils arranged on the upper side of FP_L will be slightly shorter than the distance between the rotating plate and the lower coils due to the thickness of the PCB. This results in lower sensitivity for coils on the bottom layer compared to those on the top layer. In order to solve this problem, a similar PCB FP_U was positioned above the RP in such a way that the coils on FP_L are perfectly aligned with the corresponding coils on FP_U. Each coil on FP_U are connected in anti-series with the corresponding coils FP_L and forms a net inductance of L_i (where $L_i = L_{Ui} + L_{Li} - 2M_{ULi}$, $0 \leq i \leq 4$). Here L_{Ui} is the inductance of one of the coils on FP_U, L_{Li} is the corresponding coil inductance on FP_L and M_{ULi} is the mutual inductance between them. The coils were connected this way so that the magnetic field in the space between the coils of FP_U and FP_L partially cancels out each other in the absence of the RP. In this dual PCB arrangement, the effective air gap between the RP and each coil will remain consistent across all the coils.

2) Axial Misalignment of the Shaft: Using a single PCB on one side of the RP, attached to the rotor, can lead to inaccuracies in inductance measurements if there are vertical movements (along the axis of rotation of the rotor) of the RP. Vertical movements of the rotor, caused by vibrations, pose significant challenges in automotive applications. However, this issue can be mitigated by employing the dual PCB arrangement.

In order to verify the feasibility of dual PCB arrangement, a simulation model was built and analyzed in COMSOL Multiphysics software. From FEA studies, it was observed that

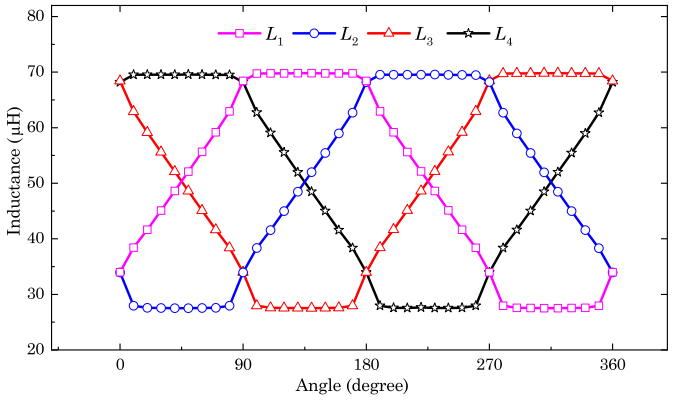

Fig. 4. Inductance variation against θ for the coils FP_1-FP_4 obtained from FEM studies.

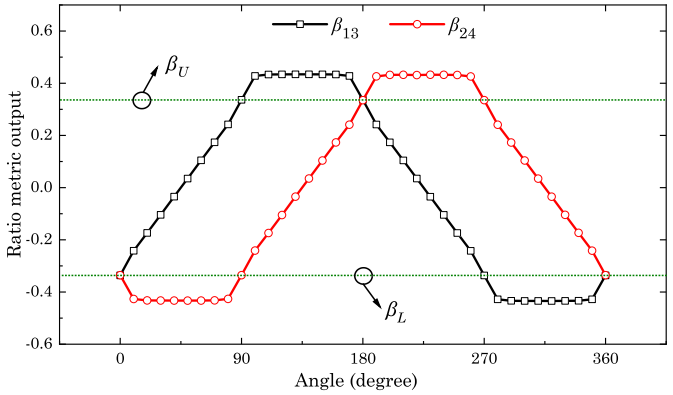

Fig. 5. The variation of ratiometric outputs, β_{13} and β_{24} obtained in FEA simulation studies, is plotted against θ. Here, β_L and β_U are the upper and lower thresholds used in algorithm described in Section III-C.

the shape of the inductance characteristics remains consistent with the rotation of the RP, regardless of whether a single coil or dual coil arrangement is employed. However, the sensitivity to inductance variation is higher for a dual coil arrangement compared to the single coil, providing an additional advantage to this system.

In FEA, the RP was moved in steps of 10°, and the corresponding inductance values L_1 to L_4 of the coils FP_1 to FP_4 were recorded for each case. These values are then plotted against θ as shown in Fig. 4. It can be seen that L_1 and L_3 vary linearly in a push-pull manner in the range 0°-90° and 180°-270°. Similarly, L_2 and L_4 vary linearly in a push-pull manner in the range 90°-180° and 270°-360°. The linearity can be further improved if we adopt the ratio-metric operation of these differential (push-pull) pairs of waveforms. However, it can be seen from Fig. 4 that, if we start from 0°, the differential pair of waveforms that needs to be used in each quadrant is different. Hence, it is necessary to develop an algorithm capable of identifying the θ by utilizing the correct ratiometric output for each quadrant obtained from the inductances.

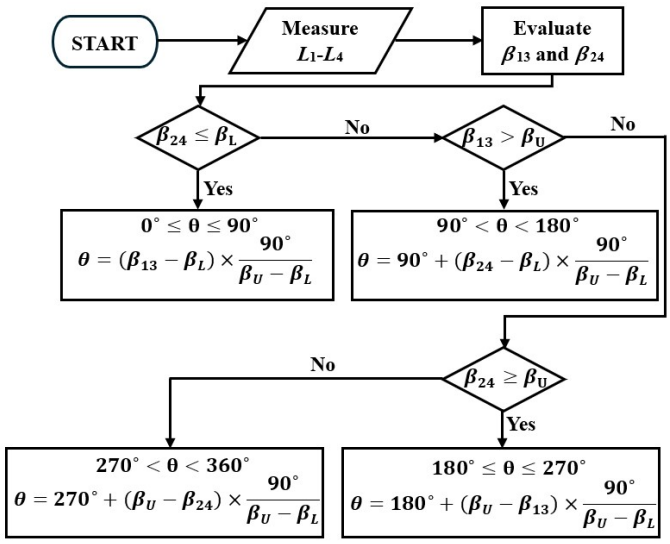

Fig. 6. Flowchart showing the algorithm to identify the quadrant and θ.

C. Algorithm for Angle Measurement

The ratiometric outputs β_{13} and β_{24}, can be obtained from coils positioned opposite to each other as:

$$\beta_{13} = \frac{L_1 - L_3}{L_1 + L_3}; \quad \beta_{24} = \frac{L_2 - L_4}{L_2 + L_4} \tag{2}$$

The use of ratiometric outputs provides the sensor system with the benefit of effectively canceling out common errors occurring in coil inductances. These errors may include drift induced by temperature changes, noise present in inductance measurements, influences from the power supply on inductance measurements, etc.

The variation of β_{13} and β_{24} against θ is plotted in Fig. 5. It shows that β_{13} increases linearly when $0° < \theta \le 90°$ and decreases linearly for $180° < \theta \le 270°$. Similarly, β_{24} linearly increases between 90° and 180° and decreases linearly between 270° and 360°. Using these properties, we can identify the θ value for the full circle range with the help of an algorithm shown in Fig. 6. In the algorithm, the constants β_L and β_U are utilized as references for the implementation of the algorithm. β_L can be determined by averaging the values of β_{13} and β_{24} at 180°. Similarly, β_U can be obtained by averaging the values of β_{13} and β_{24} at 360°. The values of β_{24} and β_{13} are less than β_L for quadrants 1 and 4 respectively. Similarly, β_{13} and β_{24} are greater than β_U for quadrants 2 and 3 respectively. This information is used to identify the quadrant in which θ lies. As shown in Fig. 6, by using the standard equation of the straight line fit of β_{13} and β_{24} in each quadrant, the θ information can be obtained.

D. Effects of variation of relative permeability (μ_r) of RP

The change in μ_r may occur in real-time applications due to the temperature fluctuations and slight variations encountered in the manufacturing of the metal in industries [14]. FEA was repeated to capture the effect of variations in μ_r of RP. The μ_r was changed from 4000 to 40,000, and the ratiometric output, β_{13}, was calculated for different θ values and is plotted in

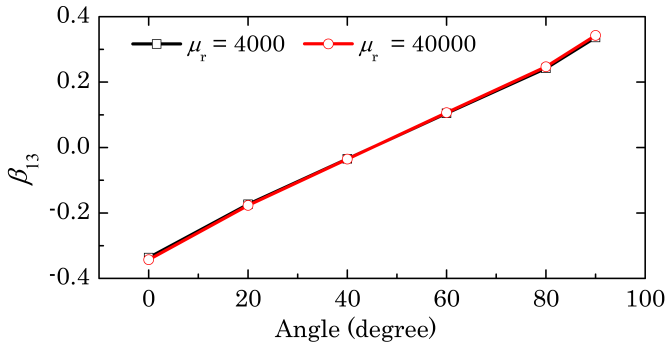

Fig. 7. The variation of ratiometric outputs, β_{13}, obtained in FEA simulation studies was plotted for two different values of relative permeability, μ_r, of 4000 and 40,000. The maximum change in θ, observed near 0° and 90° was found to be negligibly small at 2.1 %.

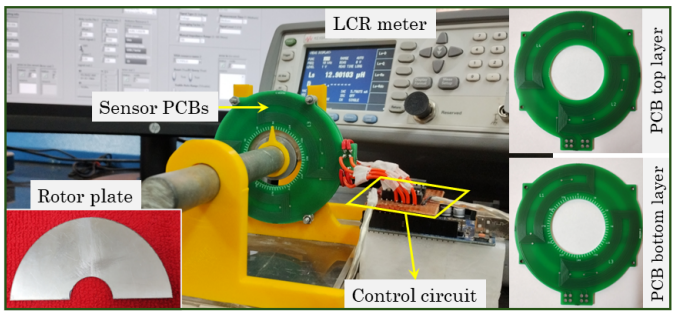

(a)

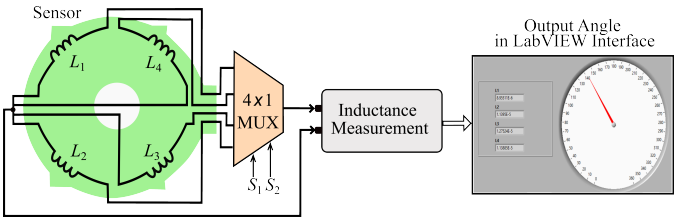

(b)

Fig. 8. (a) Photograph of the experimental set-up. The inset shows the constituent PCBs, FP_L and FP_U as well as the rotor plate (RP). (b) Measurement circuit. Here MUX represents a multiplexer.

Fig. 7. The maximum change in θ was found to be negligible at 2.1 %. This is an additional advantage of using ratiometric outputs in the proposed sensor system because of which a slight variation in the properties of the RP does not affect the sensor operation.

IV. Experimental Set-up and Results

A. Prototype Unit

A prototype of the proposed sensor system was built in the laboratory to test its efficacy. The dimensions of the prototype were decided in line with a typical industrial application, for example, steering wheel position sensor. Fig. 8a shows a photograph of the experimental test setup. As discussed in Section III-B, in order to improve the sensitivity and to reduce the effect of axial misalignment of the rotor, the sensor was fabricated using two double-sided identical PCBs (FP_U and FP_L) one for upper coil set and the other for bottom coil set. Each PCB has four identical planar coils (FP_{U1}-FP_{U4} and FP_{L1}-FP_{L4}) to cover the full angle range of 0°-360° (as in Section III-A). The coils were in the shape of annulus sectors placed 90° apart and arranged along the rim of a circle. Two of these coils are arranged on the top layer of the PCB, and the other two are on the bottom layer of the PCB. The upper and lower PCBs were parallelly mounted onto a fixed frame such that the corresponding coils on these PCBs are in perfect alignment. Each of the coils on the upper PCB was connected to the corresponding coils on the lower PCB (as in Section II-A). The four coils formed this way are referred to as FP_1-FP_4 and the corresponding inductances are referred to as L_1-L_4. The details of the coils on the PCB is given in Table I.

TABLE I
Sensor Prototype Design Parameters

Sensor Component	Parameter	Value
PCB	Outer diameter (d_o)	80 mm
	Inner diameter (d_i)	35 mm
	Thickness	1.6 mm
PCB Coils	Number of turns	11
	Inductance	5.53 µH
	Internal resistance	3.36 Ω
	Overhang (ϕ)	30 °
Rotor Plate	μ_r	40,000
	Outer diameter	80 mm
	Inner diameter	20 mm
	Thickness	1 mm
Aluminium Shaft	Length	250 mm
	Diameter	15 mm

The semi-circular-shaped rotor plate (RP) (shown in the inset of Fig. 8a) was manufactured using CNC machines with commercially available mu-metal sheets, and its details are listed in Table I. RP is firmly attached to the mechanical shaft, whose angle of rotation has to be measured. This is done by using a 3D printed bobbin of thickness 5 mm. The RP is placed in between FP_U and FP_L with an air gap of 0.5 mm on either side.

Fig. 8b shows the schematic diagram of the measurement circuit. L_1-L_4 shows the equivalent inductance of the coils FP_1-FP_4. An analog multiplexer IC, MAX4708, from MAXIM is used to sequentially connect the coils, one by one, for inductance measurement at each position of the RP. Each inductances were measured using LCR meter, E4980AL from keysight, at 10 kHz frequency. Once all the inductance values L_1-L_4 are measured, then θ can be calculated using the algorithm.

1) Calibration:: Ideally, the maximum inductance value and the minimum inductance value of each of the individual coils, L_1-L_4, should be the same. Also, the sloped of these inductance plots should be the same. Due to manufacturing limitations and misalignment occurring during sensor assembly, a minor deviation in the slope of the inductance plot is observed. To rectify this, a calibration process was conducted initially.

To rectify the deviation in slope of inductance plot, L_1-L_4, the measured inductances were scaled using gain factors $G_1 = 1$, $G_2 = 0.99$, $G_3 = 1$ and $G_4 = 1.03$, respectively. After this, an offset adjustment was done such that the maximum and minimum values of each coil inductances are made same.

TABLE II
PERFORMANCE COMPARISON BETWEEN SENSORS

Parameters	[14]	[7]	[20]	[13]	[21]	[12]	This work
Manufacturability	Simple	Moderate	Moderate	Complex	Complex	Moderate	Simple
Linearity (%)	0.7	1.1	0.02	0.72	0.3	< 1	0.31
Resolution	0.06 °	-	22 bits	-	0.09 °	0.15 °	0.11 °
Sensitivity to misalignment	No	Yes	Yes	Yes	Yes	No	No
Axial thickness (mm) x radial width (mm)	5×28	-	10×146	-	30×24	140×2	5.2×40
Viablility in through shaft applications	Yes	Yes	Yes	Yes	Yes	Yes	Yes
Range (°)	360	225	360	360	360	360	360
Electrical contact to the moving part	No	No	No	No	No	Yes	No

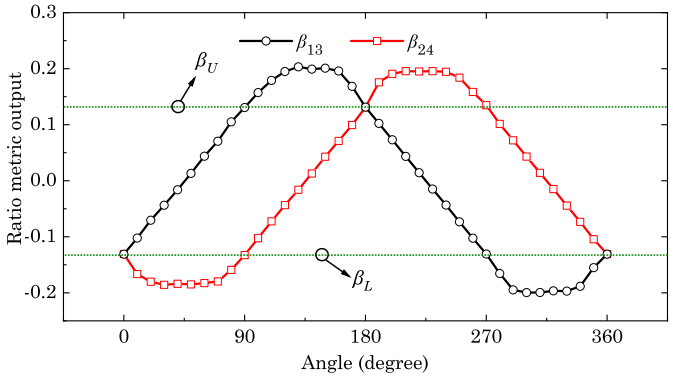

Fig. 9. The rationmetric output obtained from the prototype plotted against θ.

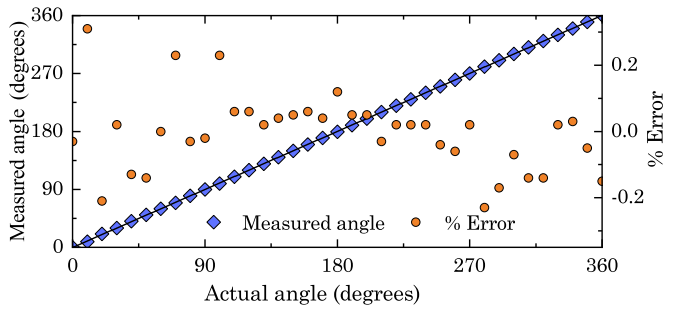

Fig. 10. Final output characteristics of measured angle and error characteristics of the sensor prototype unit.

This calibration process is a one-time requirement, necessary only once after the sensor manufacturing process.

B. Results

1) Linearity Test: After completing the calibration process, the RP was moved in steps of 10 °, and the inductance values, L_1-L_4, were measured using an LCR meter. The data obtained from the LCR meter is then processed using a virtual instrument (VI) developed using LabVIEW. From the inductance values, the ratiometric outputs, β_{13} and β_{24} are evaluated and plotted in Fig. 9. The plots show excellent agreement with the results that are obtained from FEA. As shown in Fig. 9, β_{13} shows a linear increase in 0°-90° and decreases linearly in 180°-270°. Similarly, β_{24} increases linearly in 90°-180° and decreases linearly in 270°-360°. From β_{13} and β_{24}, the angle θ is estimated using the algorithm given in Fig. 6. The measured output angle and the error characteristics are shown in Fig. 10. It is observed from the graph that the sensor exhibits excellent linearity with a worst-case non-linearity of 0.31%.

2) Repeatability Test: In order to examine the repeatability characteristics of the proposed sensor, the RP was kept fixed at 90 ° and a set of 150 readings were recorded for L_1-L_4. For each readings, β_{13} was computed. The parameters of the repeatability test was then evaluated using [22]. From the test the standard deviation (SD) and sensitivity of β_{13} were evaluated as 0.0003 and 0.0029/°, respectively. The repeatability error was found to be 0.0005 %. The resolution of the sensor system was found to be 0.11 °.

3) Effect of Axial Misalignment: Any axial misalignment of the shaft can lead to a variation in core position. To quantify the effect of axial misalignment on the measured angle, the test was repeated by taking angle measurements after intentionally introducing a core misalignment of ± 1 mm. For this test, the sensor prototype was reassembled with an increased air gap between the RP and PCBs. It was observed that there was minimal error in angle measurement, with the worst- case error of 0.57 %.

4) Effect of the Presence of External Magnetic Material: The presence of a magnetic object in proximity to the sensor coils will change their inductances. To assess this impact, a magnetic plate (μ_r=40,000), with a sector shape spanning 120° and a thickness of 2 mm was placed externally near one of the PCBs of the sensor prototype. The clearance between the sensor prototype and the external magnetic plate was 5 mm. The angle measurement at a particular angle of 270° was repeated for different positions of the external magnetic plate. It was observed that the worst-case error in angle measurements is 0.76 %.

To further minimize the error, a magnetic shield was employed outside the sensor prototype. The magnetic shield should be made of a material with good permeability for better shielding. Higher the relative permeability, better the shielding. However, depending on the cost constraints on the sensor design, one may use a low permeable material, with a trade off on shielding capability. The experiment was then repeated with the magnetic shield placed between the sensor PCB and the external magnetic plate. The magnetic shield used had a relative permeability of 40,000 with a thickness of the shield plate being 0.2 mm. It was observed that the worst-case error decreased to 0.37 %.

It can be concluded that the use of a suitable casing with magnetic shielding will effectively reduce the impact of exter-

nal magnetic and conductive materials on angle measurements. Additionally, the use of ratiometric calculation in the output helps to mitigate these effects.

5) Effect of the Stray Capacitance: In practical applications of the proposed sensor, the presence of parasitic capacitance may introduce measurement errors. To assess their impact on apparent inductance values in real-world circuits, we investigated various potential sources of parasitic capacitance. This included 1. capacitance arising out of the sensing element such as lead capacitance and interwinding capacitance of the coil, capacitance between the top PCB and bottom PCB of the sensor etc. 2. Capacitances arising from measurement circuitry like cables, wires, and PCB traces. The analysis indicated minimal capacitance ($< 13\,\mathrm{pF}$) from sensing element. Here, the use of planar coils helped in minimizing parasitic effects. In addition, the operating frequency of $10\,\mathrm{kHz}$ is carefully selected in such a way that it is much below (around 300 times) the self resonant frequency (SRF) of the coils. This ensures minimal sensitivity to the parasitic capacitances. To minimize the effects of parasitic capacitance arising from measurement circuit, additional steps are required which includes adapting or designing signal conditioning circuits that are less sensitive to parasitic capacitances, utilizing shielded cables and proper grounding techniques and so forth.

V. Discussions

The sensor presented in this paper is well suited in through-shaft applications where the available longitudinal space is limited, for example, steering wheel sensing and brake wear sensing. Moreover, the proposed sensor can be used in CNC machines and 3D printers to control and monitor the spindle unit's position. However, there are existing angle sensors that are suitable for the application mentioned above. Therefore, a comparison study is inevitable to quantify the advantages and disadvantages of the proposed sensor. Table II shows a comparative study of the proposed sensor with the existing inductive angle sensors, where the comparison parameters are carefully chosen in terms of performance, features, and practical importance.

The comparison study shows that the proposed sensor system offers superior linearity and resolution over a full circle measurement range of 0°-360°. Moreover, it is easy to manufacture and less sensitive to axial misalignment of the shaft. It can be clearly inferred from Table II that the proposed sensor has many advantages, such as (1) high resolution, (2) good linearity, (3) no electrical contact to the rotor, (4) requires very less longitudinal space, and (5) insensitivity to misalignment.

The experiment results show excellent tolerance to the axial misalignment of the shaft. Additionally, the sensor is immune to interference from external magnetic material. These properties underscore the sensor's reliability and effectiveness in real-world applications, particularly when considering challenges such as misalignment and external magnetic interference.

VI. Conclusion

A novel planar angle sensor, based on the variable reluctance sensing principle and characterized by good linearity and simple manufacturing procedures, is built and presented in this paper. The proposed sensor system utilizes two parallel plate PCBs with a semi-circular rotor plate positioned in between. The rotor plate is attached to the rotating shaft, whose angle needs to be measured. Each of the PCBs has four constituent coils, which are in the shape of an annulus sector. As the rotor plate rotates, the inductances of the coils are modulated as a function of θ. An algorithm was designed to estimate the rotor angle based on the inductance values. Initially, an analytical study along with FEM simulation analysis was performed to understand the operational principle of the sensor system. Subsequently, a laboratory-scale prototype was built to validate the proposed design. From the experimental studies, the performance of the sensor was validated. The test results show excellent linearity of $0.31\,\%$ and a good resolution of $0.11\,^\circ$. The dual PCB structure employed in the system ensures the sensor is immune to any axial misalignment of the shaft, making it the right choice for automotive and industrial applications. Moreover, its negligible sensitivity to external magnetic objects enhances its suitability for industrial use.

References

[1] W. J. Fleming, "Overview of automotive sensors," *IEEE Sensors J.*, vol. 1, no. 4, pp. 296–308, Jan. 2001.

[2] A. S. A. Kumar, B. George, and S. C. Mukhopadhyay, "Technologies and applications of angle sensors: A review," *IEEE Sensors J.*, vol. 21, no. 6, pp. 7195–7206, Mar. 2021.

[3] T. Hara, K. Asamura, Y. Nagata, and S. Nagasawa, "Stacked electrostatic angle sensor implemented in micro robot leg joints," *Japanese Journal of Applied Physics*, vol. 60, no. SC, p. SCCL08, mar 2021. [Online]. Available: https://dx.doi.org/10.35848/1347-4065/abe5c0

[4] X. Zhu, W. Liu, J. Qian, H. Zhuang, W. Zhang, J. Cao, G. Zhang, Y. Yang, Y. Cai, Y. Shi, and W. Wu, "A novel wearable knee joint angle monitoring sensor utilizing mach–zehnder interferometer with triple-clad fiber," *IEEE Sensors J.*, vol. 24, no. 3, pp. 2785–2791, 2024.

[5] S. Umesh, S. Padma, T. Srinivas, and S. Asokan, "Fiber bragg grating goniometer for joint angle measurement," *IEEE Sensors J.*, vol. 18, no. 1, pp. 216–222, 2018.

[6] N. Anandan and B. George, "A wide-range capacitive sensor for linear and angular displacement measurement," *IEEE Trans. Ind. Electron.*, vol. 64, no. 7, pp. 5728–5737, Jul. 2017.

[7] C. S. Anoop and B. George, "A new variable reluctance-Hall effect based angle sensor," in *Proc. 6th Int. Conf. Sens. Technol. (ICST)*, Dec. 2012, pp. 454–459.

[8] S. Wang, Z. Wu, D. Peng, S. Chen, Z. Zhang, and S. Liu, "Sensing mechanism of a rotary magnetic encoder based on time grating," *IEEE Sensors J.*, vol. 18, no. 9, pp. 3677–3683, May 2018.

[9] K. B. Nandapurkar, A. C. Sreekantan, and P. K. Dutta, "Performance investigation of a simplified TMR-based rotary position sensing system," *IEEE Trans. Instrum. Meas.*, vol. 70, pp. 1–8, Jan. 2021.

[10] C. S. Anoop, B. George, and V. J. Kumar, "Analysis of a tunnelling magneto-resistance-based angle transducer," *IET Circuit, Devices & Systems*, vol. 8, no. 4, pp. 301–310, 2014.

[11] R. Pallas-Areny and J. G. Webster, *Sensors and signal conditioning.*, Hoboken, NJ, USA: Wiley 2000.

[12] N. Anandan, A. A. V. Muppala, and B. George, "A flexible, planar-coil-based sensor for through-shaft angle sensing," *IEEE Sensors J.*, vol. 18, no. 24, pp. 10 217–10 224, Dec. 2018.

[13] Melexis. Inductive resolver for e-motor, e-brake and e-steering. [Online]. Available: https://www.melexis.com/en/tech-talks/inductive-resolver-for-e-motor-e-brake-and-e-steering

[14] A. S. A. Kumar, B. George, and S. C. Mukhopadhyay, "Design and development of a variable reluctance-based thin planar angle sensor," *IEEE Trans. Ind. Electron.*, vol. 70, no. 9, pp. 9653–9662, Sep. 2023.

[15] F. Tootoonchian and F. Zare, "Presentation of a novel absolute variable-reluctance tubular resolver," *IEEE Trans. Instrum. Meas.*, vol. 72, pp. 1–8, 2023.

[16] H. Saneie, Z. Nasiri-Gheidari, and F. Tootoonchian, "Accuracy improvement in variable reluctance resolvers," *IEEE Trans. Energy Convers.*, vol. 34, no. 3, pp. 1563–1571, Sep. 2019.

[17] A. S. A. Kumar and B. George, "A non-contact angle sensor based on eddy current technique," *IEEE Trans. Instrum. Meas.*, vol. 69, no. 4, pp. 1275–1283, Apr. 2020.
[18] N.-k. J. Kitazawa, Kanji Iida-shi, "Variable-reluctance-type angle sensor," European Patent Office Patent EP 0 802 398 B1, Jun. 14, 2000.
[19] X. Ge, Z. Zhu, R. Ren, and J. Chen, "A novel variable reluctance resolver for hev/ev applications," in *2015 IEEE International Electric Machines Drives Conference (IEMDC)*, 2015, pp. 611–617.
[20] Y. Wang, Y. Qin, X. Chen, Q. Tang, T. Zhang, and L. Wu, "Absolute inductive angular displacement sensor for position detection of YRT turntable bearing," *IEEE Trans. Ind. Electron.*, vol. 69, no. 10, pp. 10 644–10 655, Oct. 2022.
[21] *Inductive Angle Sensor With Analog Output RI360P1-QR14-LIU5X2*, TURCK Works: Industrial Automation, 9 2017.
[22] L. Xu, S. Sun, Z. Cao, and W. Yang, "Performance analysis of a digital capacitance measuring circuit," *Rev. Sci. Instrum.*, vol. 86, no. 5, p. 054703, 2015.